Journal of Stress Analysis
Vol. 6, No. 1, Spring – Summer 2021, 139-156
Bu-Ali Sina University

ORIGINAL RESEARCH PAPER

Low-Velocity Impact Response Analysis of Laminated Composite Cylindrical Shells Subjected to Combined Pre-Loads

A. Davar, R. Azarafza*, J. Eskandari Jam, A. Labbafian Mashhadi
Faculty of Materials and Manufacturing Technologies, Malek Ashtar University of Technology, Tehran, Iran.

Article info

Article history:
Received 29 July 2021 Received in revised form
13 September 2021
Accepted 18 September 2021

Keywords:
Low-velocity impact
Composite cylindrical shells
Mechanical pre-loads
Thermal pre-loads

Abstract

In this paper, the low-velocity impact response of laminated composite cylindrical shells subjected to the combined pre-loads is investigated. The pre-load is applied as the mechanical pre-load (axial force and radial pressure) and the thermal pre-load. The boundary conditions are considered as simply supported and the behavior of the material is linear-elastic. The equations are based on the first-order shear deformation theory and the Fourier series method is used to solve the analytical equations. The impactor studied as a large mass and therefore the impact response is considered to be quasi-static. The results show that regardless of the type of the axial pre-load (tensile or compressive), changes in contact parameters during the impact are linearly related to the temperature changes. Furthermore, these variations with respect to the radial pressure is almost linear for the tensile axial pre-load, but it is nonlinear for the compressive axial pre-load.

Nomenclature

$u, v, w, \psi_x, \psi_\varphi$	Displacement components	ω_{mn}	Natural circular frequency
$x_1, x_2, \varphi_1, \varphi_2$	Edge coordinates of area of applied load	I_1, I_2, I_3	Mass moments of inertia
$N_x, N_\varphi, N_x\varphi$	Normal force resultants	K_{bs}	Equivalent bending-shear stiffness
Q_x, Q_φ	Shear force resultants	K_c^*	Characteristic contact stiffness
$N_x^t, N_\varphi^t, N_{x\varphi}^t$	Thermal force resultants	K_c	Contact stiffness
$M_x^t, M_\varphi^t, M_{x\varphi}^t$	Thermal moment resultants	M_i	Impactor mass
$q_x, q_\varphi, q_z, m_x, m_\varphi$	External excitations	M_s^*	Equivalent shell mass
$\varepsilon_x^0, \varepsilon_\varphi^0, \varepsilon_{x\varphi}^0$	Middle surface in-plane strains	$\gamma_{xz}^0, \gamma_{\varphi z}^0$	Out-of-plane shear strains
$\mathbf{A}_{ij}, \mathbf{B}_{ij}, \mathbf{D}_{ij}, \mathbf{H}_{ij}$	Stiffness matrices	$2l_1, 2l_2$	Size of the area of applied load
$A_{mn}, B_{mn}, C_{mn}, D_{mn}, E_{mn}$	Displacement Fourier constants	$T_{mn}(t)$	Generalized coordinate with respect to time
$E_1, E_2, G_{12}, G_{13}, G_{23}, \upsilon_{12}$	Material mechanical properties	ω_1, ω_2	Natural frequencies of two-degree-of-freedom (TDOF) spring-mass system
$\alpha_x, \alpha_\varphi, \alpha_{x\varphi}$	Thermal expansion coefficients in off-axis coordinates	m, n	Wave numbers in axial and tangential directions
$M_x, M_\varphi, M_x\varphi$	Moment resultants	q_0	Uniform pressure magnitude

*Corresponding author: R. Azarafza (Associate Professor)
E-mail address: azarmut@mut.ac.ir
http://dx.doi.org/10.22084/jrstan.2021.24816.1191
ISSN: 2588-2597

x, φ, z	Coordinate system components	ΔT	Temperature difference
R	Radius	t	Time
P_{cr}	Critical buckling pressure	P_{mn}	Load Fourier constants
N_a	Axial force per unit length	$\bar{J}_{mn}$	Normalized mass
P	Lateral pressure	$G_{mn}(t)$	Generalized force
L_{ij}	Differential operators	p	Unit transverse force
$F_c(t)$	Contact force (function of time)	$x_s(t)$	Shell transverse displacement
α_1, α_2	Thermal expansion coefficients in on-axis coordinates	l_x, l_φ	Length of the cylindrical panel straight and curved edges
N_{cr}	Critical buckling axial force	V_0	Impact velocity
γ	Subtended angle of the cylindrical panel	R_i	Impactor radius
R_{eff}	Effective contact radius	ΔT_{cr}	Critical buckling temperature difference
E_{eff}	Effective contact Young's modulus	ω_f	Fundamental frequency
x_l, φ_l	Impact point coordinates	$\bar{\omega}$	Dimensionless frequency parameter

1. Introduction

Composite cylindrical shells are one of the most widely used parts in various industries due to their very high properties and very low weight. Composite structures may be subjected to a variety of impact loads in their work environment. Applying a small impact load can cause a large deformation and, ultimately, damage to the structure. This is more dangerous in composite structures because damage to composite structure may occur in the inner layers and the appearance of the structure does not indicate this damage; meanwhile, the composite structure can be subjected to pre-loads in its environmental conditions that affect the impact response. Therefore, it is very important to know the response of the shell to the impact and how the pre-loads affect it.

Many researchers have tried to predict the low-velocity impact response in composite plates and shells. Gong et al. [1] investigated the linear behavior of cylindrical laminated panels subjected to low-velocity impact. Using a spring-mass system, they considered the impactor and the shell as two rigid objects and their contact stiffness and bending stiffness of the shell as two springs, and by solving the equation of motion of this system, they determined the displacement of the shell and the contact force. Toh et al. [2] using a higher-order shear deformation theory analyzed the transient low-velocity impact response of orthotropic laminated cylindrical panels. Matemilola and Stronge [3] developed an analytical solution for the impact response of a simply supported anisotropic composite cylinder. In their analysis, the contact force was obtained from the compatibility condition between the elastic impactor and the cylinder, with a modified Hertzian law. Abrate [4] categorized the types of models proposed for impact analysis on composite structures and stated the scope and the range of application of each model. He divided the types of models for impact analysis on composite structures into four groups: energy balance model, spring-mass model, complete model, and impact model on infinite plates. Her and Liang [5], using the ANSYS/LS-DYNA finite element software, studied the composite laminate and shell structures subjected to low-velocity impact. Kumar et al. [6] studied the impact response and the impact-induced damage in a curved composite laminates subjected to transverse impact using a three-dimensional finite element method. Saghafi et al. [7] experimentally investigated the effect of pre-lead on the impact response of curved composite panels. Choi [8] investigated the transient responses of a composite laminated plate and cylindrical shells subjected to low-velocity impacts numerically. He used the shear deformation theory of a doubly curved shell and von Karman's large deflection theory to develop a geometrically nonlinear finite element program. Najafi et al. [9] presented a nonlinear investigation for impact response of Functionally Graded Material (FGM) doubly curved panels resting on Winkler–Pasternak elastic foundation with simply supported end conditions. Rafiee et al. [10] presented theoretical and numerical analyses of composite cylinders subjected to the low-velocity impact. Langella et al. [11] investigated the influence of a tensile pre-load on the impact behavior of thin woven composite laminates. Harris et al. [12] presented the results of drop-weight impact testing on curved $\pm 55^\circ$ E-glass/Epoxy laminates of varying radii and wall thickness. Liao et al. [13] studied the residual burst strength of composite pressure vessels after low-velocity impact using an explicit-implicit combined model. Rafiee et al. [14] developed a theoretical study of failure in composite pressure vessels subjected to low-velocity impact and internal pressure.

In this paper, the low-velocity impact response of composite cylindrical shells in presence of the mechanical and thermal pre-loads is investigated analytically. The mechanical pre-loads are applied as the tensile or compressive axial loads and the internal or external pressure. The thermal loads are applied by applying a uniformly distributed temperature difference to the entire shell. Accordingly, as a new feature of the present

work, based on the existing analytical formulation in the literature, the effect of the thermal and mechanical combined pre-loads on the low-velocity impact response on the composite cylindrical shells is investigated for the first time. New interesting results have been obtained hitherto not reported in the literature.

2. Governing Equations

Fig. 1 shows a cylindrical shell with radius R, thickness h, axial length l_x, circumferential length l_φ and central angle γ, and the reference coordinates. The middle surface of the shell is considered as the reference surface, and the x, φ, and z coordinate system is placed on it. Moreover, u, v and w are the displacement components in the axial (x), circumferential (φ) and radial (z) directions, respectively, and indicate the deformation of the shell.

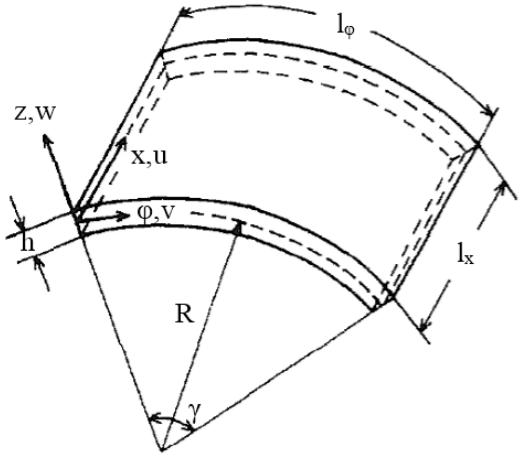

Fig. 1. Cylindrical shell and coordinate system located on the reference surface [15].

Based on the First-order Shear Deformation Theory (FSDT), the equations of motion of a composite cylindrical shell subjected to axial load N_a, internal pressure P and thermal in-plane loads N_x^t, N_φ^t and $N_{x\varphi}^t$ are as follows [16, 17]:

$$\frac{\partial N_x}{\partial x}+\frac{1}{R}\frac{\partial N_{x\phi}}{\partial \varphi}+P\left(\frac{1}{R}\frac{\partial^2 u}{\partial \varphi^2}+\frac{\partial w}{\partial x}\right)+q_x(x,\varphi,t) = I_1\frac{\partial^2 u}{\partial t^2}+I_2\frac{\partial^2 \psi_x}{\partial t^2}$$

$$\frac{\partial N_{x\varphi}}{\partial x}+\frac{1}{R}\frac{\partial N_\varphi}{\partial \varphi}+\frac{Q_\varphi}{R}+(N_a-N_x^t)\frac{\partial^2 v}{\partial x^2}+P\left(\frac{1}{R}\frac{\partial^2 v}{\partial \varphi^2}+\frac{\partial w}{\partial \varphi}\right)+q_\varphi(x,\varphi,t) = \left(I_1+\frac{2I_2}{R}\right)\frac{\partial^2 v}{\partial t^2}+\left(I_2+\frac{I_3}{R}\right)\frac{\partial^2 \psi_\varphi}{\partial t^2}$$

$$\frac{\partial Q_x}{\partial x}+\frac{1}{R}\frac{\partial Q_\varphi}{\partial \varphi}-\frac{N_\varphi}{R}+(N_a-N_x^t)\frac{\partial^2 w}{\partial x^2}-2N_{x\varphi}^t\frac{1}{R}\frac{\partial^2 w}{\partial x\partial \varphi^2}-N_\varphi^t\frac{1}{R^2}\frac{\partial^2 w}{\partial \varphi^2}-P\left(\frac{\partial u}{\partial x}-\frac{\partial v}{R\partial \varphi}-\frac{\partial^2 w}{R\partial \varphi^2}\right)+q_z(x,\varphi,t) = I_1\frac{\partial^2 w}{\partial t^2}$$

$$\frac{\partial M_x}{\partial x}+\frac{1}{R}\frac{\partial M_{x\varphi}}{\partial \varphi}-Q_x+m_x(x,\varphi,t) = I_3\frac{\partial^2 \psi_x}{\partial t^2}+I_2\frac{\partial^2 u}{\partial t^2}$$

$$\frac{\partial M_{x\varphi}}{\partial x}+\frac{1}{R}\frac{\partial M_\varphi}{\partial \varphi}-Q_\varphi+m_\varphi(x,\varphi,t) = I_3\frac{\partial^2 \psi_x}{\partial t^2}+\left(I_2+\frac{I_3}{R}\right)\frac{\partial^2 v}{\partial t^2} \tag{1}$$

where ψ_x and ψ_φ are the cross-sectional clockwise rotations around the φ and x axes, respectively, q_x, q_φ and q_z are external forces and m_x and m_φ are external moments applied to the shell. The terms of inertia, I_1, I_2, and I_3 are defined by the following equations [16]:

$$(I_1, I_2, I_3) = \int_{-h/2}^{h/2}(1, z, z^2)\rho_k dz \tag{2}$$

where ρ_k is the density of each layer. In Eq. (1) the stress resultants $\{\mathbf{N}\}^T = \{N_x, N_\varphi, N_{x\varphi}\}$, moments $\{M\}T = \{M_x, M_\varphi, M_{x\varphi}\}$, and transverse shear forces $\{Q\}^T = \{Q_x, Q_\varphi\}$ are defined as follows [16, 18]:

$$\begin{Bmatrix} \mathbf{N} \\ \mathbf{M} \end{Bmatrix} = \begin{bmatrix} \mathbf{A} & \mathbf{B} \\ \mathbf{B} & \mathbf{D} \end{bmatrix}\begin{Bmatrix} \mathbf{e} \\ \boldsymbol{\kappa} \end{Bmatrix} - \begin{Bmatrix} \mathbf{N}^t \\ \mathbf{M}^t \end{Bmatrix}, \quad \{\mathbf{Q}\} = [\mathbf{H}]\begin{Bmatrix} \gamma_{xz}^0 \\ \gamma_{\varphi z}^0 \end{Bmatrix} \tag{3}$$

where $\mathbf{A}, \mathbf{B}, \mathbf{D}$, and $\mathbf{H}$ are the extensional, coupling, bending and thickness shear stiffness matrices, respectively and defined as follows [16]:

$$(\mathbf{A_{ij}}, \mathbf{B_{ij}}, \mathbf{D_{ij}}) = \int_{-h/2}^{h/2}(1, z, z^2)\bar{\mathbf{Q}}_{\mathbf{ij}}dz \quad (i,j=1,2,6)$$

$$\mathbf{H_{ij}} = k_0\int_{-h/2}^{h/2}\bar{\mathbf{Q}}_{\mathbf{ij}}dz \quad (i,j=4,5) \tag{4}$$

where k_0 is the shear correction factor introduced by Mindlin and is equal to $\pi^2/12$ and $\bar{\mathbf{Q}}_{\mathbf{ij}}$ is the transformed reduced stiffness matrix.

In Eq. (3), $\{\mathbf{e}\}^T = \{\varepsilon_x^0, \varepsilon_\varphi^0, \varepsilon_{x\varphi}^0\}$ is the vector of the mid-surface engineering strains, γ_{xz}^0 and $\gamma_{\varphi z}^0$ are the transverse shear strains, and $\{\kappa\}^T = \{\kappa_x, \kappa_\varphi, \kappa_{x\varphi}\}$ is the vector of the curvature and twist of the shell defined as follows [16]:

$$\{\varepsilon_x^0, \varepsilon_\varphi^0, \gamma_{x\varphi}^0\} = \left\{\frac{\partial u}{\partial x}, \frac{1}{R}\frac{\partial v}{\partial \varphi}+\frac{w}{R}, \frac{1}{R}\frac{\partial u}{\partial \varphi}+\frac{\partial v}{\partial x}\right\}$$

$$\{\kappa_x, \kappa_\varphi, \kappa_{x\varphi}\} = \left\{\frac{\partial \psi_x}{\partial x}, \frac{1}{R}\frac{\partial \psi_\varphi}{\partial \varphi}, \frac{1}{R}\frac{\partial \psi_x}{\partial \varphi}+\frac{\partial \psi_\varphi}{\partial x}\right\}$$

$$\{\gamma_{xz}^0, \gamma_{\varphi z}^0\} = \left\{\psi_x+\frac{\partial w}{\partial x}, \psi_\varphi+\frac{1}{R}\frac{\partial w}{\partial \varphi}-\frac{v}{R}\right\} \tag{5}$$

Additionally, the strains at any distance from the mid-surface are obtained from the following equations [18]:

$$\begin{aligned}\varepsilon_x &= \varepsilon_x^0 + z\kappa_x \\ \varepsilon_\varphi &= \varepsilon_\varphi^0 + z\kappa_\varphi \\ \gamma_{x\varphi} &= \gamma_{x\varphi}^0 + z\kappa_{x\varphi} \\ \gamma_{xz} &= \gamma_{xz}^0 \\ \gamma_{\varphi z} &= \gamma_{\varphi z}^0\end{aligned} \tag{6}$$

The thermal stress resultants $\{\mathbf{N^t}\}^T = \{N_x^t, N_\varphi^t, N_{x\varphi}^t\}$ and moments $\{\mathbf{M}^t\}^T = \{M_x^t, M_\varphi^t, M_{x\varphi}^t\}$ are obtained from the following equations [17]:

$$\begin{Bmatrix} N_x^t \\ N_\varphi^t \\ N_{x\varphi}^t \end{Bmatrix} = \int_{-h/2}^{h/2} \mathbf{\bar{Q}_{ij}} \begin{Bmatrix} \alpha_x \\ \alpha_\varphi \\ \alpha_{x\varphi} \end{Bmatrix} \Delta T dz \quad (i,j = 1,2,6)$$

$$\begin{Bmatrix} M_x^t \\ M_\varphi^t \\ M_{x\varphi}^t \end{Bmatrix} = \int_{-h/2}^{h/2} \mathbf{\bar{Q}_{ij}} \begin{Bmatrix} \alpha_x \\ \alpha_\varphi \\ \alpha_{x\varphi} \end{Bmatrix} \Delta T z dz \quad (i,j = 1,2,6) \tag{7}$$

where ΔT is the temperature difference and α_x, α_φ and $\alpha_{x\varphi}$ are the coefficients of thermal expansion in off-axis directions, which are related to the coefficients of thermal expansion in the on-axis directions, α_1 and α_2, as follows [18]:

$$\begin{Bmatrix} \alpha_x \\ \alpha_\varphi \\ \alpha_{x\varphi/2} \end{Bmatrix} = [\mathbf{T}]^{-1} \begin{Bmatrix} \alpha_1 \\ \alpha_2 \\ 0 \end{Bmatrix} \tag{8}$$

where $[\mathbf{T}]$ is the transformation matrix.

According to the definitions provided in Eqs. (3) to (8) and substituting in Eq. (1) the equations of motion can be simplified as follows:

$$\begin{bmatrix} L_{11} & L_{12} & L_{13} & L_{14} & L_{15} \\ L_{21} & L_{22} & L_{23} & L_{24} & L_{25} \\ L_{31} & L_{32} & L_{33} & L_{34} & L_{35} \\ L_{41} & L_{42} & L_{43} & L_{44} & L_{45} \\ L_{51} & L_{52} & L_{53} & L_{54} & L_{55} \end{bmatrix} \begin{Bmatrix} u(x,\varphi,t) \\ v(x,\varphi,t) \\ w(x,\varphi,t) \\ \psi_x(x,\varphi,t) \\ \psi_\varphi(x,\varphi,t) \end{Bmatrix}$$

$$= \begin{Bmatrix} -q_x \\ -q_\varphi \\ -q_z \\ -m_x \\ -m_\varphi \end{Bmatrix} \tag{9}$$

L_{ij} are differential operators that are listed in Appendix A for a general orthotropic shell. Because in the present study the general orthotropic shells are examined, the $N_{x\varphi}^t$ becomes zero. Furthermore, because the term N_φ^t is created outside the $[L]$, it will be ignored and therefore only the term N_x^t remains [17] and the remaining eigenvalue problem is solved.

2.1. Boundary Conditions

The boundary conditions for a fully Simply Supported Cylindrical Shell (SSSS) are defined as follows [19]:

$$\begin{aligned} x = 0, l_x \quad & v = w = N_x = M_x = \psi_\varphi = 0 \\ \varphi = 0, \gamma \quad & u = w = N_\varphi = M_\varphi = \psi_x = 0 \end{aligned} \tag{10}$$

In order to satisfy these boundary conditions, displacements and rotations are defined as the following double Fourier series [19]:

$$\begin{aligned} u &= \sum_{m=1}^{\infty}\sum_{n=1}^{\infty} A_{mn} \cos\frac{m\pi x}{l_x} \sin\frac{n\pi\varphi}{\gamma} T_{mn}(t) \\ v &= \sum_{m=1}^{\infty}\sum_{n=1}^{\infty} B_{mn} \sin\frac{m\pi x}{l_x} \cos\frac{n\pi\varphi}{\gamma} T_{mn}(t) \\ w &= \sum_{m=1}^{\infty}\sum_{n=1}^{\infty} C_{mn} \sin\frac{m\pi x}{l_x} \sin\frac{n\pi\varphi}{\gamma} T_{mn}(t) \\ \psi_x &= \sum_{m=1}^{\infty}\sum_{n=1}^{\infty} D_{mn} \cos\frac{m\pi x}{l_x} \sin\frac{n\pi\varphi}{\gamma} T_{mn}(t) \\ \psi_\varphi &= \sum_{m=1}^{\infty}\sum_{n=1}^{\infty} E_{mn} \sin\frac{m\pi x}{l_x} \cos\frac{n\pi\varphi}{\gamma} T_{mn}(t) \end{aligned} \tag{11}$$

where $A_{mn}, B_{mn}, C_{mn}, D_{mn}$, and E_{mn} are constant coefficients of mode shapes, m is the number of longitudinal half-waves, n is the number of circumferential half-waves, and $T_{mn}(t)$ is the generalized coordinates as a function of time.

2.2. Free Vibration Analysis

In order to study the free vibrations, the external loads and moments on the shell are ignored and $T_{mn}(t) = e^{-i\omega_{mn}t}$ is considered as a time function. Using Eq. (11) and substituting it in Eq. (9), the following equation system is obtained:

$$\big[[\mathbf{K}]_{mn} - \omega_{mn}^2[\mathbf{M}]_{mn}\big]\{\Delta\}_{mn} = 0 \tag{12}$$

where $\{\Delta\}_{mn} = \{A_{mn}B_{mn}C_{mn}D_{mn}E_{mn}\}^T$ is the vector of constant coefficients of mode shapes, and $[\mathbf{M}]_{mn}$ and $[\mathbf{K}]_{mn}$ are the mass matrix and stiffness matrix, respectively, given in Appendix B. By setting the determinants of the coefficients of the Eq. (12) equal to zero), the characteristic frequency equation of a composite cylindrical shell is derived as follows:

$$\delta_1\omega^{10} + \delta_2\omega^8 + \delta_3\omega^6 + \delta_4\omega^4 + \delta_5\omega^2 + \delta_6 = 0 \tag{13}$$

where δ_i, $i = 1, \cdots, 5$ are constant coefficients. This equation has 5 acceptable positive roots, the smallest one is usually related to the bending mode shape.

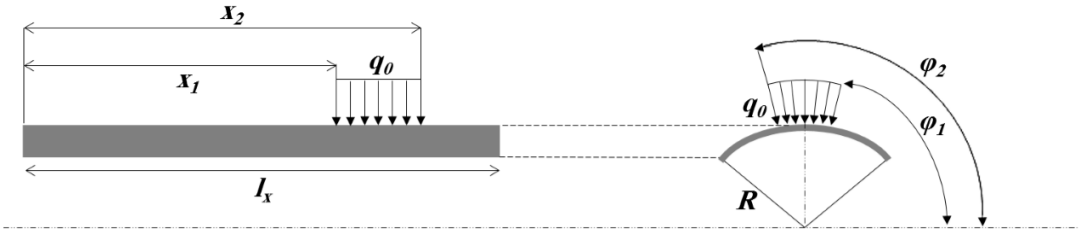

Fig. 2. Uniform static pressure applied on the outer surface of the shell.

The constant coefficients of mode shapes corresponding to each frequency determine the corresponding mode shape. In order to normalize this mode shapes relative to the mass matrix, the following equation is used [20]:

$$\int_0^{l_x}\int_0^{\gamma} \Delta_{mn}^T \mathbf{M}_{mn} \Delta_{mn} dx d\varphi = 1 \tag{14}$$

The normalized mode shapes obtained from this equation is used in the analysis of the impact dynamic response.

2.3. Buckling Analysis

In order to determine the allowable pre-loads, the buckling analysis is used. Regardless of the terms including the time and the external forces and moments in Eq. (9), the following relation is obtained:

$$[\mathbf{C}_{ij}]\{\Delta\}_{mn} = 0 \tag{15}$$

In this equation, if each of the values of the axial load, the pressure or the temperature are assumed to be unknown, by equating the determinants of the $[\mathbf{C}_{ij}]$ to zero for each m and n, an equation for the unknown axial load, pressure, or temperature is obtained. The smallest positive root of this equation for each mode (each m and n) is the axial critical buckling load, the critical buckling pressure, or the critical buckling temperature corresponded to that mode. The lowest eigenvalue corresponded to different mode numbers (m, n) determines the axial critical buckling load (N_{cr}), the critical buckling external pressure (P_{cr}) or the critical buckling temperature (ΔT_{cr}) of the shell [17, 21].

2.4. Transverse Static Load Analysis

In order to determine the global static stiffness (K_{bs}) of the shell, static analysis is required. It is assumed that only the transverse static force, q_z, is applied on the shell and according to Fig. 2, it is considered as a uniformly distributed pressure (q_0) over a rectangular surface located on the outer surface of the shell.

According to Fig. 2, the coordinates of the center point of this surface (x_l, φ_l) are defined as follows:

$$2x_l = x_1 + x_2 \quad , \quad 2\varphi_l = \varphi_1 + \varphi_2 \tag{16}$$

Moreover, the dimensions of the load application surface are defined as $A_l = 2l_1 \times 2l_2$, in which $2l_1$ and $2l_2$ are defined as follows:

$$2l_1 = R(\varphi_2 - \varphi_1) \quad , \quad 2l_2 = x_2 - x_1 \tag{17}$$

In order to satisfy the boundary conditions, the transverse load is considered as follows [22]:

$$q_z = (x, \varphi) = \sum_{m=1}^{\infty}\sum_{n=1}^{\infty} P_{mn} \sin\frac{m\pi x}{l_x} \sin\frac{n\pi\varphi}{\gamma} \tag{18}$$

where P_{mn} is the Fourier constant coefficient which depends on the profile, the size and the position of the applied load. Due to the small surface area of the impact, it is assumed that the pressure distribution on the rectangular surface is uniform of amplitude equal to q_0. For uniform pressure, P_{mn} is obtained as follows:

$$P_{mn} = \frac{4q_0}{mn\pi^2}\left(\cos\frac{m\pi x_2}{l_x} - \cos\frac{m\pi x_1}{l_x}\right) \left(\cos\frac{n\pi\varphi_2}{\gamma} - \cos\frac{n\pi\varphi_1}{\gamma}\right) \tag{19}$$

By substituting Eqs. (18) and (19) into Eq. (9) and neglecting the time, the following equation of static equilibrium is obtained:

$$[\mathbf{K}]\{\Delta\}_{mn} = \{\mathbf{q}\} \tag{20}$$

where $\{\mathbf{q}\}^T = \{0\ 0\ P_{mn} 0\ 0\}$ is the vector of the external static load. By solving this system of equations, the constants of mode shapes of the $\{\Delta\}$ are determined and according to Eq. (11), the displacement components are obtained.

2.5. Transverse Impact Response Analysis

It is assumed that a homogeneous, isotropic and elastic spherical impactor with mass M_i and initial velocity V_0 strikes perpendicular to the outer surface of the cylindrical shell as shown in Fig. 3.

In order to calculate the impact response, the external force function, q_z, is defined as follows:

$$q_z(x, \varphi, t) = q_z(x, \varphi) f(t) = \sum_{m=1}^{\infty}\sum_{n=1}^{\infty} P_{mn} \sin\frac{m\pi x}{l_x} \sin\frac{n\pi\varphi}{\gamma} f(t) \tag{21}$$

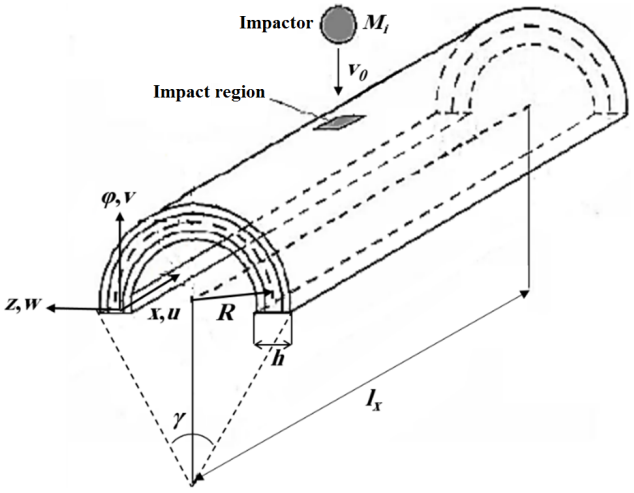

Fig. 3. Transverse impact applied to the outer surface of the shell.

where $f(t)$ is the function of time. Substituting Eqs. (21) and (11) in Eq. (9), the following relation is obtained:

$$\begin{bmatrix} L_{11} & L_{12} & L_{13} & L_{14} & L_{15} \\ L_{21} & L_{22} & L_{23} & L_{24} & L_{25} \\ L_{31} & L_{32} & L_{33} & L_{34} & L_{35} \\ L_{41} & L_{42} & L_{43} & L_{44} & L_{45} \\ L_{51} & L_{52} & L_{53} & L_{54} & L_{55} \end{bmatrix} \begin{Bmatrix} \bar{A}_{mn} \\ \bar{B}_{mn} \\ \bar{C}_{mn} \\ \bar{D}_{mn} \\ \bar{E}_{mn} \end{Bmatrix} T_{mn}(t) \tag{22}$$

$$= \begin{Bmatrix} \ddot{T}_{mn}(t)(I_1\bar{A}_{mn} + I_2\bar{D}_{mn}) \\ \ddot{T}_{mn}(t)\left[\left(I_1 + \dfrac{2I_2}{R}\right)\bar{B}_{mn} + \left(I_2 + \dfrac{I_3}{R}\right)\bar{E}_{mn}\right] \\ \ddot{T}_{mn}(t)(I_1\bar{C}_{mn}) - q_z(x,\varphi,t) \\ \ddot{T}_{mn}(t)(I_3\bar{D}_{mn} + I_2\bar{A}_{mn}) \\ \ddot{T}^{(t)}_{mn}\left[I_3\bar{E}_{mn} + \left(I_2 + \dfrac{I_3}{R}\right)\bar{B}_{mn}\right] \end{Bmatrix}$$

in which the vectors of the mode shape functions are defined as follows:

$$\begin{Bmatrix} \bar{A}_{mn} \\ \bar{B}_{mn} \\ \bar{C}_{mn} \\ \bar{D}_{mn} \\ \bar{E}_{mn} \end{Bmatrix} = \begin{Bmatrix} A_{mn}\cos\dfrac{m\pi x}{l_x}\sin\dfrac{n\pi\varphi}{\gamma} \\ B_{mn}\sin\dfrac{m\pi x}{l_x}\cos\dfrac{n\pi\varphi}{\gamma} \\ C_{mn}\sin\dfrac{m\pi x}{l_x}\sin\dfrac{n\pi\varphi}{\gamma} \\ D_{mn}\cos\dfrac{m\pi x}{l_x}\sin\dfrac{n\pi\varphi}{\gamma} \\ E_{mn}\sin\dfrac{m\pi x}{l_x}\cos\dfrac{n\pi\varphi}{\gamma} \end{Bmatrix} \tag{23}$$

Using the free vibration equations ($T_{mn}(t) = e^{i\omega_{mn}t}$), the left side of the Eq. (22) can be substituted as follows:

$$\begin{bmatrix} L_{11} & L_{12} & L_{13} & L_{14} & L_{15} \\ L_{21} & L_{22} & L_{23} & L_{24} & L_{25} \\ L_{31} & L_{32} & L_{33} & L_{34} & L_{35} \\ L_{41} & L_{42} & L_{43} & L_{44} & L_{45} \\ L_{51} & L_{52} & L_{53} & L_{54} & L_{55} \end{bmatrix} \begin{Bmatrix} \bar{A}_{mn} \\ \bar{B}_{mn} \\ \bar{C}_{mn} \\ \bar{D}_{mn} \\ \bar{E}_{mn} \end{Bmatrix} T_{mn}(t)$$

$$= -\omega^2_{mn}T_{mn}(t) \begin{Bmatrix} I_1\bar{A}_{mn} + I_2\bar{D}_{mn} \\ \left(I_1 + \dfrac{2I_2}{R}\right)\bar{B}_{mn} + \left(I_2 + \dfrac{I_3}{R}\right)\bar{E}_{mn} \\ I_1\bar{C}_{mn} \\ I_3\bar{D}_{mn} + I_2\bar{A}_{mn} \\ I_3\bar{E}_{mn} + \left(I_2 + \dfrac{I_3}{R}\right)\bar{B}_{mn} \end{Bmatrix} \tag{24}$$

By substituting Eq. (24) in Eq. (22), the following relations are obtained:

$$\begin{aligned}
&-\omega^2_{mn}T_{mn}(t)(I_1\bar{A}_{mn} + I_2\bar{D}_{mn}) = \ddot{T}_{mn}(t)(I_1\bar{A}_{mn} + I_2\bar{D}_{mn}) \\
&-\omega^2_{mn}T_{mn}(t)\left[\left(I_1 + \frac{2I_2}{R}\right)\bar{B}_{mn} + \left(I_2 + \frac{I_3}{R}\right)\bar{E}_{mn}\right] \\
&\quad = \ddot{T}_{mn}(t)\left[\left(I_1 + \frac{2I_2}{R}\right)\bar{B}_{mn} + \left(I_2 + \frac{I_3}{R}\right)\bar{E}_{mn}\right] \\
&-\omega^2_{mn}T_{mn}(t)(I_1\bar{C}_{mn}) = \ddot{T}_{mn}(t)(I_1\bar{C}_{mn}) - q_z(x,\varphi,t) \\
&-\omega^2_{mn}T_{mn}(t)(I_3\bar{D}_{mn} + I_2\bar{A}_{mn}) = \ddot{T}_{mn}(t)(I_3\bar{D}_{mn} + I_2\bar{A}_{mn}) \\
&-\omega^2_{mn}T_{mn}(t)\left[I_3\bar{E}_{mn} + \left(I_2 + \frac{I_3}{R}\right)\bar{B}_{mn}\right] \\
&= \ddot{T}_{mn}(t)\left[I_3\bar{E}_{mn} + \left(I_2 + \frac{I_3}{R}\right)\bar{B}_{mn}\right]
\end{aligned} \tag{25}$$

Multiplying the sides of the Eq. (25) in $\bar{A}_{mn}, \bar{B}_{mn}, \bar{C}_{mn}, \bar{D}_{mn}$, and $\bar{E}_{mn}$, respectively, and after adding the equations, the following equation is obtained:

$$\ddot{T}_{mn}(t)\bar{N}_{mn} + \omega^2_{mn}T_{mn}(t)\bar{N}_{mn} = \bar{C}_{mn}q_z(x,\varphi,t) \tag{26}$$

where $\bar{N}_{mn}$ is as follows:

$$\begin{aligned}
\bar{N}_{mn} &= I_1(\bar{A}^2_{mn} + \bar{B}^2_{mn} + \bar{C}^2_{mn}) \\
&\quad + I_2(2\bar{A}_{mn}\bar{D}_{mn} + 2\bar{B}_{mn}\bar{E}_{mn} + \frac{2}{R}\bar{B}^2_{mn}) \\
&\quad + I_3(\bar{D}^2_{mn} + \bar{E}^2_{mn} + \frac{2}{R}\bar{B}_{mn}\bar{E}_{mn})
\end{aligned} \tag{27}$$

By sorting the Eq. (26) and integrating with respect to x and φ from its sides, a typical second-order differential equation in terms of the time is obtained as follows:

$$\ddot{T}_{mn}(t) + \omega^2_{mn}T_{mn}(t) = G_{mn}(t) \tag{28}$$

where $G_{mn}(t)$ is the generalized forces as follows:

$$G_{mn}(t) = \frac{\int_0^{l_x}\int_0^{\gamma} \bar{C}_{mn} q_z(x,\varphi,t) dx d\varphi}{\bar{J}_{mn}} \quad (29)$$

where $\bar{J}_{mn}$ is the normalized masses as follows:

$$\bar{J}_{mn} = \int_0^{l_x}\int_0^{\gamma} \{I_1(\bar{A}_{mn}^2 + \bar{B}_{mn}^2 + \bar{C}_{mn}^2) + I_2(2\bar{A}_{mn}\bar{D}_{mn} + 2\bar{B}_{mn}\bar{E}_{mn} + \frac{2}{R}\bar{B}_{mn}^2) + I_3(\bar{D}_{mn}^2 + \bar{E}_{mn}^2 + \frac{2}{R}\bar{B}_{mn}\bar{E}_{mn})\} dx d\varphi \quad (30)$$

By substituting Eq. (29) into Eq. (28) and some simplifications, the following equation is obtained:

$$\ddot{T}_{mn}(t) + \omega_{mn}^2 T_{mn}(t) = \frac{P_{mn} C_{mn} f(t)}{J_{mn}} \quad (31)$$

where J_{mn} is the normalized mass defined as follows:

$$J_{mn} = I_1(A_{mn}^2 + B_{mn}^2 + C_{mn}^2) + I_2\left(2A_{mn}D_{mn} + 2B_{mn}E_{mn} + \frac{2}{R}B_{mn}^2\right) + I_3\left(D_{mn}^2 + E_{mn}^2 + \frac{2}{R}B_{mn}E_{mn}\right) \quad (32)$$

Using the Laplace transformation and according to the convolution integral, the solution of Eq. (32) for zero initial conditions is achieved as follows:

$$T_{mn}(t) = \frac{P_{mn} C_{mn}}{J_{mn}\omega_{mn}} \int_0^t f(\tau) \sin \omega_{mn}(t-\tau) d\tau \quad (33)$$

According to superposition principle, the time response of the cylindrical shell is obtained by replacing $T_{mn}(t)$ from Eq. (33) into Eq. (11).

3. Definition the Impact Time Function

In order to determine the time function of the contact force, a Two-Degree-of-Freedom (TDOF) spring-mass model is used. To prepare the initial information, first the static deflection of the shell under a concentrated unit force (p) is obtained at a point with coordinates (x_1, φ_1) from static analysis. In order to apply concentrated force, the load application area must be considered as a small square. Since the central impact is considered in this paper, by placing the coordinates of the center of the shell in the following equation, the global static stiffness of the shell, K_{bs}, is obtained as follows:

$$K_{bs} = \frac{p}{w(x_1, \varphi_1)} \quad (34)$$

The natural frequencies of the shell are also calculated for each mode shape number (m, n) and the smallest of them is defined as the fundamental frequency, ω_f. By considering the impactor and the shell as two rigid masses and two springs according to Fig. 4, the equation of motion of this two-degree-of-freedom system using Newton's second law is obtained as follows:

$$\begin{bmatrix} M_i & 0 \\ 0 & M_s^* \end{bmatrix} \begin{Bmatrix} \ddot{x}_i \\ \ddot{x}_s \end{Bmatrix} + \begin{bmatrix} K_c^* & -K_c^* \\ -K_c^* & (K_c^* + K_{bs}) \end{bmatrix} \begin{Bmatrix} x_i \\ x_s \end{Bmatrix} = \begin{Bmatrix} 0 \\ 0 \end{Bmatrix} \quad (35)$$

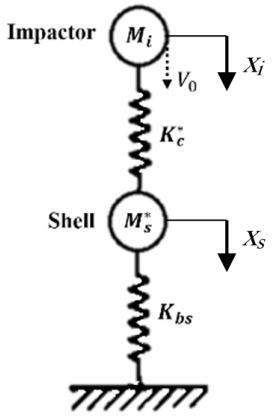

Fig. 4. Schematic of the Two-Degree-of-Freedom (TDOF) model.

where M_s^* is the effective shell mass, K_c^* is the effective (modified) contact stiffness and x_i and x_s are the impactor and shell displacement, respectively. Swanson [23] provided an approximate equation for effective mass estimation as follows:

$$\omega_f \approx \sqrt{\frac{K_{bs}}{M_s^*}} \quad (36)$$

The effective mass (the only unknown parameter) is calculated from Eq. (36) and is used in the present TDOF model. By solving Eq. (35) the contact force, $F_c(t)$, is obtained as follows:

$$F_c(t) = K_{bs} x_s(t) = \frac{K_{bs} V_0 (K_c^* - M_i\omega_2^2)(K_c^* - M_i\omega_1^2)}{K_c^* M_i(\omega_1^2 - \omega_2^2)} \times \left(\frac{\sin(\omega_1 t)}{\omega_1} - \frac{\sin(\omega_2 t)}{\omega_2}\right) \quad (37)$$

where ω_1 and ω_2 are the natural frequencies of the two-degree-of-freedom spring-mass system. In order to calculate the effective contact stiffness, the Hertz contact stiffness is first calculated as follows [4]:

$$K = \frac{4}{3} E_{eff} R_{eff}^{1/2}$$

$$\frac{1}{R_{eff}} = \frac{1}{R_1} + \frac{1}{R_2}$$

$$\frac{1}{E_{eff}} = \frac{1-\nu_1^2}{E_1} + \frac{1-\nu_2^2}{E_2} \tag{38}$$

where subscript 1 denotes the properties of the impactor and subscript 2 denotes the properties of the target structure. For the composite shell, E_{22} and υ_{12} are replaced by E_2 and υ_2, respectively. Because when impact occurs between the impactor and the target, the properties of the top layer of the target that is in contact with the impactor must be included in the equations of contact law. In fact, regardless of the number and sequence of the laminate layers, only the properties of the top (outer most) layer in contact with the external impactor is included in the contact stiffness relation, Eq. (38). Then, an iterative scheme is used to calculate the effective contact stiffness. In the first iteration, the maximum contact force is determined as [24]:

$$F_m^{(1)} = V_0\sqrt{K_{bs}M_i} \tag{39}$$

Then the contact stiffness is obtained as follows [24]:

$$K_c = F_m^{1/3}K^{2/3} \tag{40}$$

Using this contact stiffness, the maximum contact force can be recalculated from Eq. (37). This action is repeated until the maximum contact force in the i$^{\text{th}}$ iteration ($F_m^{(i)}$) does not change. The speed of convergence in this cycle is very fast. Finally, the effective contact stiffness (K_c^*) is calculated and by replacing it in Eq. (37), the time function of the contact force is obtained.

4. Finite Element Simulation

In order to validate the impact results, in addition to the available references, ABAQUS finite element software is also used. The impactor is simulated as Analytical Rigid and Conventional Shell, S4R elements are used for composite shell, and the Quad-Free meshing technique is applied. For discretizing the shell, according to Fig. 5, the meshing method presented in Ref. [25] is used. Penalty Contact method is used to simulate the contact between the impactor and the shell. The vertical contact behavior is considered as Hard Contact and the tangential contact behavior is defined as frictionless. The boundary conditions of the shell are fully simply supported. By defining the cylindrical coordinate system x, φ and z as ABAQUS coordinate system 3, 2 and 1, respectively, at the smooth edges of the shell, all the degrees of freedom except U2 (according to the term $N\varphi = 0$ in Eq. 10) and UR3 (according to the term $M\varphi = 0$ in Eq. 10) are set to be zero and at the curved edges of the shell, all the degrees of freedom except U3 (according to the term $N_x = 0$ in Eq. (10)), and UR2 (according to the term $M_x = 0$ in Eq. (10)) are set to be zero. Furthermore, the impactor can only be moved in the direction of impact. The axial pre-load is applied as Shell Edge Load, the initial pressure is applied as pressure, and the temperature difference is applied using predefined field. Moreover, since the purpose of this paper is to find the contact force prior to any damage occurrence in the structure, very small damage at the impact region is ignored and the simulation does not include damage in the shell.

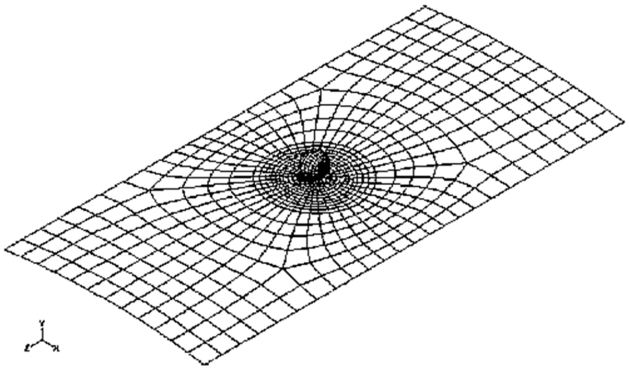

Fig. 5. The mesh pattern used in shell finite element model [25].

5. Validation of the Results

In order to validate the results, first the results of the free vibration, the critical axial buckling load, the critical external buckling pressure, the critical buckling temperature and the static analysis are compared with the results in the references then the contact force and the deflection calculated from the TDOF model and the deflection calculated from the dynamic response analysis are validated.

The fundamental frequency for a [90/0] composite cylindrical shell with $l_\varphi = 0.5R$, $R = 40h$, $E_1 = 25E_2$, $G_{12} = G_{13} = G_{23} = 0.5E_2$ and $\upsilon_{12} = 0.25$ is calculated and compared with the results obtained from Ref. [26] and Ref. [27]. The results presented in Table 1 are the dimensionless fundamental frequency parameter as follows:

$$\bar{\omega} = \omega_f l_\varphi^2\sqrt{\rho/E_2h^2} \tag{41}$$

Table 1
Dimensionless fundamental frequency parameter calculated from the analytical equations compared with the results obtained from references.

l_x/l_φ	Ref. [27]	Ref. [26]	Present
1	11.84	11.45	11.57
2	7.25	7.16	7.26
3	6.39	6.41	6.48
4	6.11	6.16	6.21
5	5.59	6.04	6.10

Table 2
Properties of the materials used in Ref. [28].

Material	E_{11} (GPa)	E_{22} (GPa)	G_{12} (GPa)	υ_{12}	Ply thickness (mm)
Graphite/epoxy	132	10.8	5.65	0.24	0.127
Kevlar/epoxy	76.8	5.5	2.07	0.34	0.127
E-glass/epoxy	38.6	8.27	4.14	0.26	0.127

The critical axial buckling load of a $[0/90]_{2s}$ composite circular cylindrical shell with $R = 0.2$m for three different materials is investigated. The properties of these three materials are given in Table 2. The results are given in Table 3 and compared with the results obtained by Ref. [28]. The numbers in parentheses indicate the mode number of critical axial buckling load (m, n).

Table 3
Critical axial buckling load (kN/m) calculated from the present method compared with the results obtained by Ref. [28].

Material	l_x/R	Ref. [28]	Present
Graphite/epoxy	1	83.02 (3,11)	83.13 (3,11)
	3	83.02 (9,11)	83.13 (9,11)
Kevlar/epoxy	1	38.69 (3,10)	38.77 (3,10)
	2	38.25 (5,10)	38.30 (5,10)
E-glass/epoxy	1	42.48 (3,12)	42.51 (3,12)
	3	42.48 (9,12)	42.51 (9,12)

The critical external buckling pressure for an isotropic circular cylindrical shell with $R/h = 300$, $E = 200$GPa and $\upsilon = 0.3$ for different l_x/R ratios is shown in Table 4 and compared with the results obtained by Ref. [21]. The numbers in parentheses indicate the mode number of critical external buckling pressure (m, n).

Table 4
Critical external buckling pressure (kPa) calculated from the present method compared with the results obtained by Ref. [21].

l_x/R	Ref. [21]	Present
0.5	276.62 (1,30)	275.94 (1,30)
1	126.96 (1,22)	126.67 (1,22)
2	60.73 (1,16)	60.61 (1,16)
3	40.72 (1,14)	40.63 (1,14)
5	23.53 (1,10)	23.48 (1,10)

The critical buckling temperature for an isotropic circular cylindrical shell with $l_x = R = 1$m, $\upsilon = 70$GPa, $\upsilon = 0.3$ and $\alpha = 23e-6/°$C is shown in Table 5 and compared with the results obtained by Ref. [29].

The static deflection of [90/0] composite cylindrical shell with $l_x = l_\varphi$, $h = 0.1l_x$, $E_1 = 25E_2$, $G_{12} = G_{13} = 0.5E_2$, $G_{23} = 0.2E_2$ and $\upsilon_{12} = 0.25$ is calculated and compared with the results obtained by Ref. [27]. The results presented in Table 6 are the dimensionless transverse deflection as follows:

$$w^* = 10^3 E_2 h^3 w/(q_0 l_x^4) \tag{42}$$

where q_0 is the uniform pressure applied to the entire outer surface of the shell. A good agreement is obtained according to Table 6.

Table 5
Critical buckling temperature (°C) calculated from the present method compared with the results obtained by Ref. [29].

h/R	Ref. [21]	Present
0.004	75.40	71.92
0.006	112.30	107.23
0.008	149.20	142.60
0.010	192.51	177.31
0.012	221.39	211.45
0.014	259.89	246.94

Table 6
Dimensionless transverse deflection calculated from the present method compared with the results obtained by Ref. [30].

l_x/R	Ref. [30]	Present	Discrepancy (%)
0.5	17.188	17.850	3.85
1	12.751	13.289	4.22
2	5.949	6.177	3.83

The contact force and the deflection calculated from the TDOF model and the deflection calculated from the dynamic response analysis for composite cylindrical shell with layup $[45/0/-45/90]_s$, $l_x = 0.254$m, $l_\varphi = 0.127$m, $R = 0.381$m, $h = 0.001$m, $E_1 = 137.8$GPa, $E_2 = 8.96$GPa, $G_{12} = G_{13} = 5.99$GPa, $G_{23} = 3.51$GPa, $\upsilon_{12} = 0.3$ and $\rho = 1590$kg/m^3 are shown in Table 7 and compared with the results obtained from the present ABAQUS simulation and geometrically linear results reported by Ref. [31]. Additionally, the shell is not generally orthotropic and contains values A_{16}, A_{26}, D_{16}, and D_{26} in its stiffness matrix. However, in many practical cases the laminates have sufficient number of plies to ignore these small values [32]. In this case, the impactor is considered as a steel sphere with $R_i = 0.00635$m and $M_i = 1.13$kg and initial velocity of $V_0 = 1.093$m/s.

In this section, the results of impact response on the composite shell in the presence of the mechanical (axial load and pressure) and the thermal pre-loads are compared with the results of ABAQUS numerical simulation. The shell lay-up is considered as $[0/90]_{2s}$, $l_x = R = 0.2$m, $h = 0.002$m, $\gamma = \pi$rad, $E_1 = 181$GPa, $E_2 = 10.3$GPa, $\upsilon_{12} = 0.28$, $G_{12} = G_{13} = 7.17$GPa, $G_{23} = 6.21$GPa, $\rho = 1600$kg/m^3, $\alpha_1 = 0.02e-6/°$C, and $\alpha_2 = 22.5e-6/°$C. Critical buckling values calculated for this shell are $N_{cr} = 412.709$kN/m, $P_{cr} = 482.951$kPa and $\Delta T_{cr} = 700°$C.

Table 7
Impact response calculated from the TDOF model and the dynamic response analysis compared with the results obtained from the present ABAQUS simulation and Ref. [31].

	Max. contact force (N)	Max. deflection (mm)	Contact time (ms)
Ref. [31]	340	3.9	11.5
Present TDOF model	334.49	4.03	11.68
Present dynamic response	334.49	4.13	11.83
Present ABAQUS	356.89	4.06	11.62

Table 8
Convergence study for the two parameters m and n in Fourier series.

m, n	10	15	20	25	50	100	150
Max. force (N)	734.3	653.97	636.97	625.98	612.32	607.74	605.69
Max. deflection (mm)	0.649	0.735	0.755	0.770	0.787	0.795	0.797

The applied pre-load on the shell is always less than the critical buckling values. The impactor is a steel sphere with $R_i = 0.00635$m, $M_i = 2$kg and $V_0 = 0.5$m/s. The relative position of the impactor and the shell and the shell mesh pattern are shown in Fig. 6. Furthermore, the convergence study for the two parameters m and n in Fourier series is given in Table 8. According to this Table, mode number $m = n = 100$ is sufficient for convergence in the analytical solution.

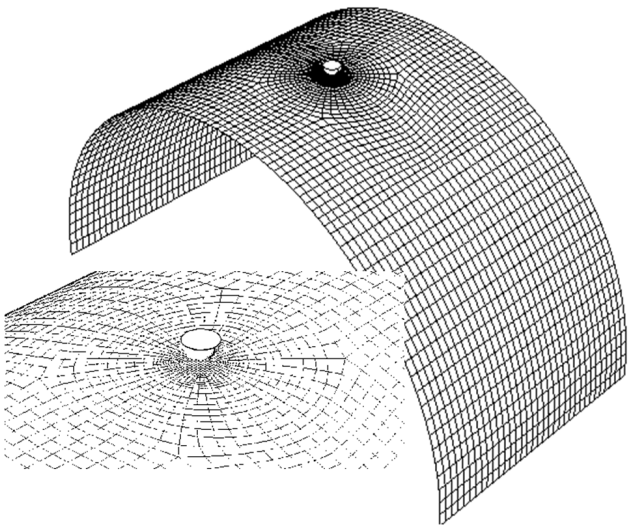

Fig. 6. Relative position of the impactor and the shell and shell mesh pattern.

The contact force and the deflection of the shell calculated from the analytical results in comparison with the results of the numerical simulation of ABAQUS are shown in Figs. 7 and 8. As can be seen, there is a good agreement between the results.

The shell response in the presence of the tensile and compressive axial pre-load using the TDOF model compared with ABAQUS results are shown in Figs. 9 and 10. The applied tensile and compressive pre-load are ±200kN/m. As can be seen from these figures, there is a good agreement between the results of the analytical equations for predicting the response of the shell under the low-velocity impact with the mean value of the results of the ABAQUS numerical simulation. The fluctuations in ABAQUS response is due to the reflected waves during contact interfering the interaction between the impactor and the shell.

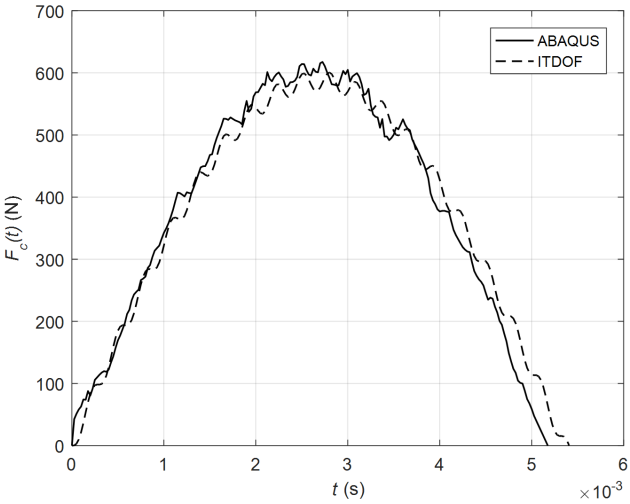

Fig. 7. Contact force calculated from the present TDOF model compared with ABAQUS.

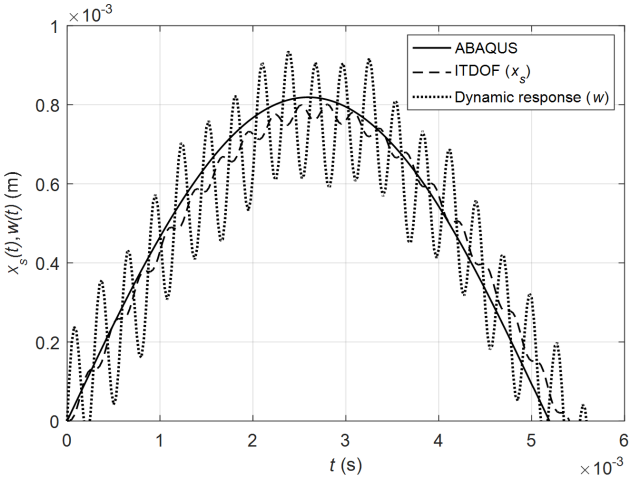

Fig. 8. Deflection of the shell calculated from the present analytical method compared with ABAQUS.

Figs. 11 and 12 show the contact force and the deflection of the shell at the impact point in the presence of 100kPa internal and external pressure from the an-

alytical result and numerical simulation of ABAQUS. As can be seen from these figures, although the pressure causes fluctuations in the contact force obtained by ABAQUS, the maximum contact force, the maximum deflection, and the contact time in presence of the internal and external pressure calculated from analytical equations and ABAQUS results are in good agreement. By applying the internal pressure, the overall stiffness of the cylindrical shell and the contact force increase and the maximum deflection decreases accordingly. Vice versa, by applying the external pressure, the overall stiffness of the cylindrical shell decreases and the contact force is decreased and the maximum deflection increses accordingly.

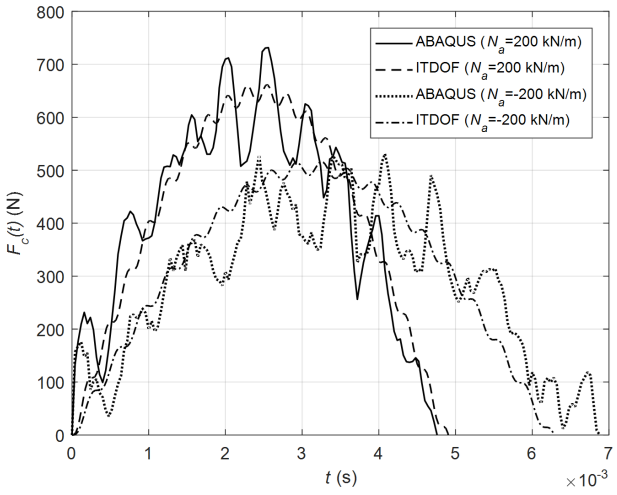

Fig. 9. Contact force calculated from the TDOF model compared with ABAQUS in presence of the tensile and compressive axial pre-loads.

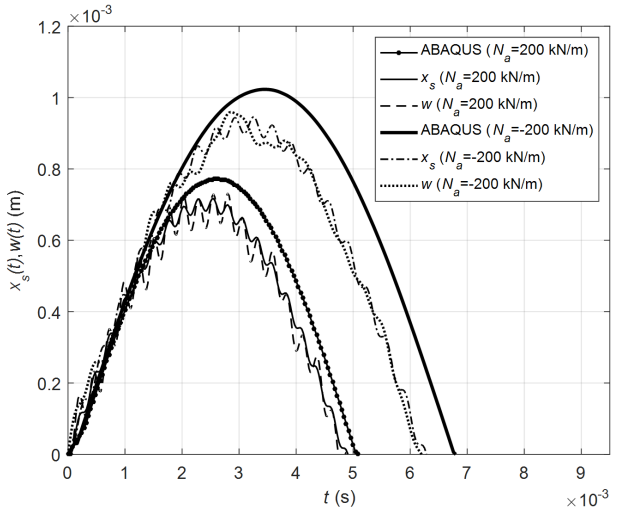

Fig. 10. Deflection of the shell calculated from the TDOF model compared with ABAQUS in presence of the tensile and compressive axial pre-loads.

The contact force and the deflection of the shell in the presence of the initial temperature difference of $\Delta T = \pm 200°\text{C}$ calculated from the analytical equations are shown in Figs. 13 and 14 and compared with the results obtained by the numerical simulation using ABAQUS. The effect of the temperature on the maximum contact force, the maximum deflection and the contact time obtained from the analytical equations and the numerical simulation of ABAQUS are in a good agreement.

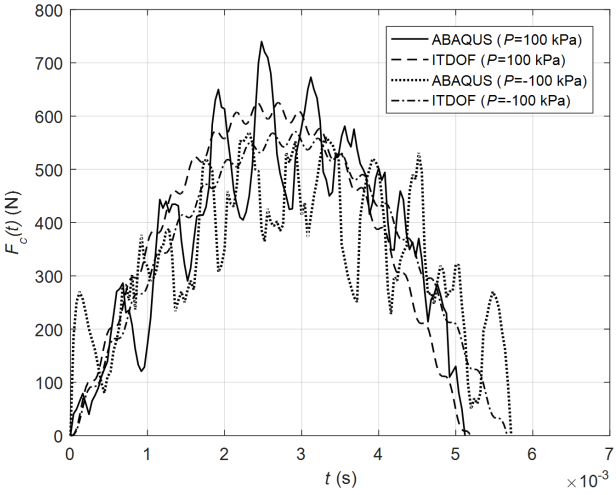

Fig. 11. Contact force calculated from the TDOF model compared with ABAQUS in presence of the internal and external pressure.

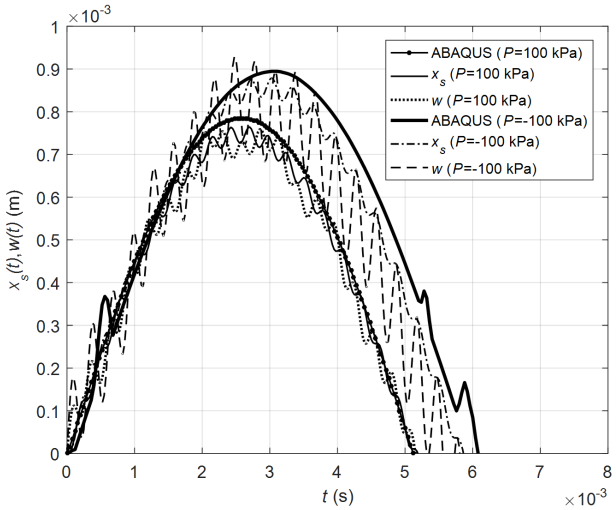

Fig. 12. Deflection of the shell calculated from the TDOF model compared with ABAQUS in presence of the internal and external pressure.

6. Numerical Results and Discussion

The impact response on the cylindrical shell in the presence of the combined pre-loads is investigated. The specifications of the shell and the impactor are considered as in the previous section. The axial preload is considered to be constant and it is equal to $N_a = \pm 200\text{kN/m}$ and the effect of temperature difference and the pressure changes are examined. In this

section, the deflection of the TDOF model is used.

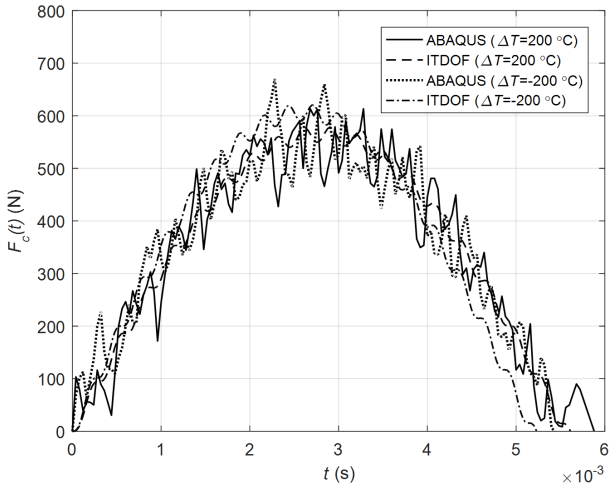

Fig. 13. Contact force calculated from the TDOF model compared with ABAQUS in presence of the temperature.

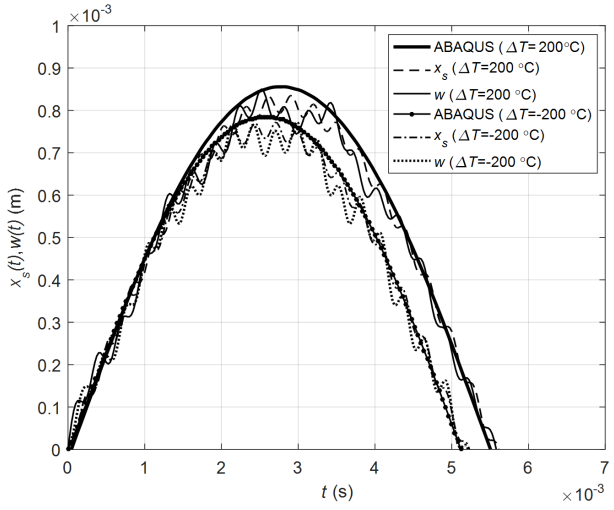

Fig. 14. Deflection of the shell calculated from the TDOF model compared with ABAQUS in presence of the temperature.

Figs. 15 and 16 show the shell response in the presence of the tensile pre-load $N_a = \pm 200$kN/m and different temperature differences. These results are also summarized in Table 9. As can be seen from this table, the temperature changes influence the shell response. However, the positive temperature difference causes the maximum contact force to decrease by 1.21% and the maximum deflection increase by 1.53%. By applying a positive temperature difference, the contact time increases by 1.02%. By applying a positive temperature difference, negative (compressive) initial stresses occur and the overall stiffness of the shell decreases. Vice versa, by applying a negative temperature difference, positive (tensile) initial stresses occur and the overall stiffness of the shell is increases.

By applying the compressive pre-load, $N_a = -200$kN/m, the shell response for different temperature differences is shown in Figs. 17 and 18. These results are also summarized in Table 10. By comparing the results of the compressive and tensile pre-loads at a certain temperature, it is concluded that the tensile pre-load causes the contact force to increase and the deflection and the duration of the contact to decrease, while the compressive pre-load causes the contact force to decrease and the deflection and the contact time to increase. By applying a positive temperature difference in the presence of the compressive pre-load, the maximum contact force decreases by 4.76%, the maximum deflection increases by 3.06% and the contact time increases by 3.85%. The negative temperature difference causes the maximum contact force to increase by 2.8%, the maximum deflection to decrease by 4.2% and the contact time decreases by 2.4%. Similar to Figs. 15 and 16, regardless of the sign of the initial mechanical stress, N_a, the overall stiffness of the shell changes by applying either positive or negative temperature differences.

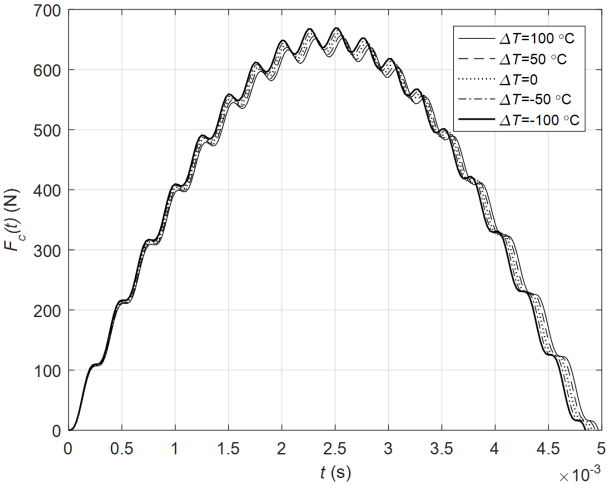

Fig. 15. Contact force in presence of the tensile pre-load $N_a = 200$kN/m and different temperature differences.

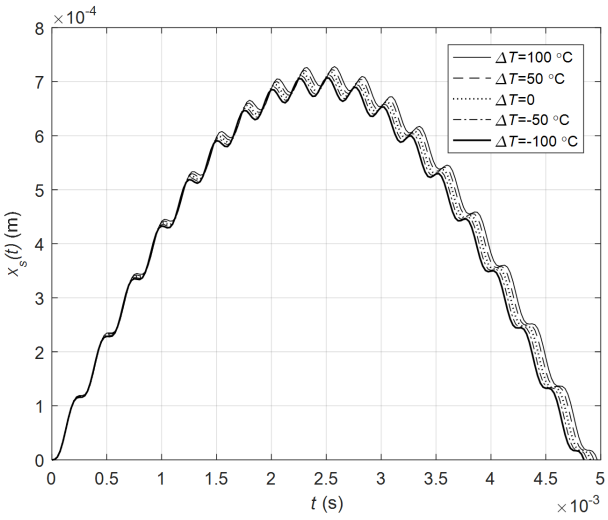

Fig. 16. Deflection of the shell in presence of the tensile pre-load $N_a = 200$kN/m and different temperature differences.

Table 9
Impact response of the shell in presence of the tensile pre-load $N_a = 200$kN/m and different temperature differences.

ΔT (°C)	Curve	Contact time (ms)	Max. force/deflection
100	F_c-t	4.975	653.324N
	x_s-t	4.975	0.728mm
50	F_c-t	4.950	657.179N
	x_s-t	4.950	0.722mm
0	F_c-t	4.925	661.334N
	x_s-t	4.925	0.717mm
-50	F_c-t	4.900	665.638N
	x_s-t	4.900	0.712mm
-100	F_c-t	4.850	668.882N
	x_s-t	4.850	0.707mm

Table 10
Impact response of the shell in presence of the compressive pre-load $N_a = 200$kN/m and different temperature differences.

ΔT (°C)	Curve	Contact time (ms)	Max. force/deflection
100	F_c-t	6.500	499.757N
	x_s-t	6.500	0.979mm
50	F_c-t	6.400	507.955N
	x_s-t	6.400	0.961mm
0	F_c-t	6.300	516.038N
	x_s-t	6.300	0.946mm
-50	F_c-t	6.200	523.628N
	x_s-t	6.200	0.930mm
-100	F_c-t	6.125	531.104N
	x_s-t	6.125	0.916mm

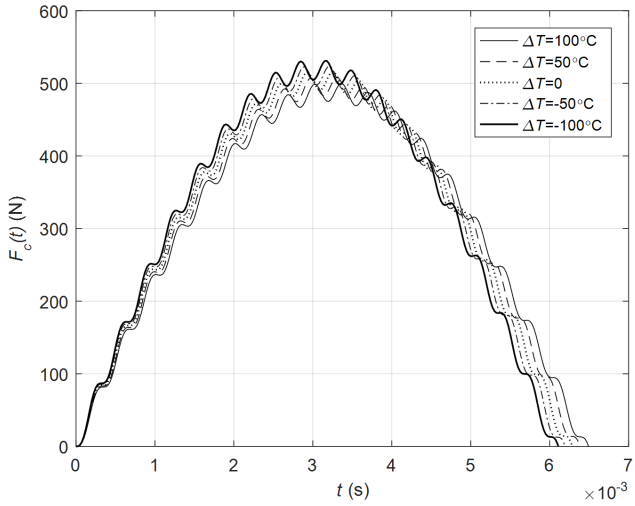

Fig. 17. Contact force in presence of the compressive pre-load N¬a=-200 kN/m and different temperature differences.

The effect of different pressures on the shell response in the presence of tensile pre-load $N_a = 200$kN/m is shown in Figs. 19 and 20 and the maximum numerical values are shown in Table 11. According to these results, the presence of internal pressure 200kPa increases the contact force by 5.96% and decreases the deflection and contact time by 6.56% and 7.57%, respectively, while the external pressure −200kPa decreases the contact force by 7.81% and increases the deflection and contact time by 9.91% and 8.12%, respectively. As described in Figs. 11 and 12, the overall stiffness of the shell increases by applying the internal pressure, and decreased by applying the external pressure. Accordingly, the impact response changes.

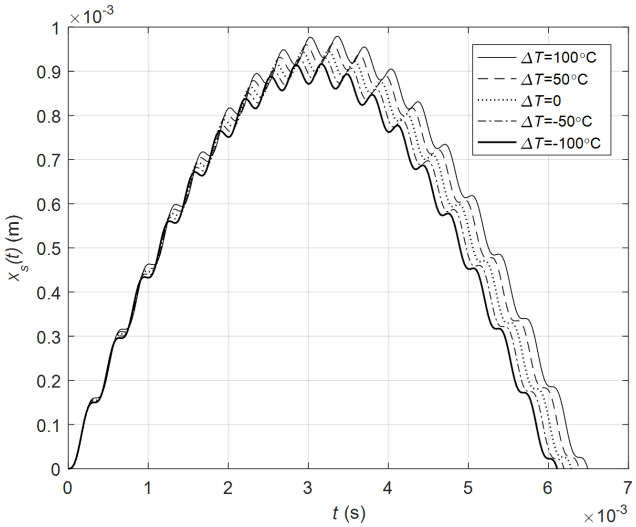

Fig. 18. Deflection of the shell in presence of the compressive pre-load $N_a = -200$kN/m and different temperature differences.

Table 11
Impact response of the shell in presence of the tensile pre-load $N_a = 200$kN/m and different pressures.

P (kPa)	Curve	Contact time (ms)	Max. force/deflection
200	F_c-t	4.575	700.726N
	x_s-t	4.575	0.670mm
100	F_c-t	4.775	682.112N
	x_s-t	4.775	0.692mm
0	F_c-t	4.925	661.334N
	x_s-t	4.925	0.717mm
-100	F_c-t	5.075	637.571N
	x_s-t	5.075	637.571mm
-200	F_c-t	5.325	609.608N
	x_s-t	5.325	0.788mm

Table 12
Impact response of the shell in presence of the compressive pre-load $N_a = -200$kN/m and different pressures.

P (kPa)	Curve	Contact time (ms)	Max. force/deflection
200	F_c-t	5.625	577.862N
	x_s-t	5.625	0.836mm
100	F_c-t	5.900	550.352N
	x_s-t	5.900	0.882mm
0	F_c-t	6.300	516.038N
	x_s-t	6.300	0.946mm
-100	F_c-t	6.875	471.500N
	x_s-t	6.875	1.045mm
-200	F_c-t	8.025	398.860N
	x_s-t	8.025	1.243mm

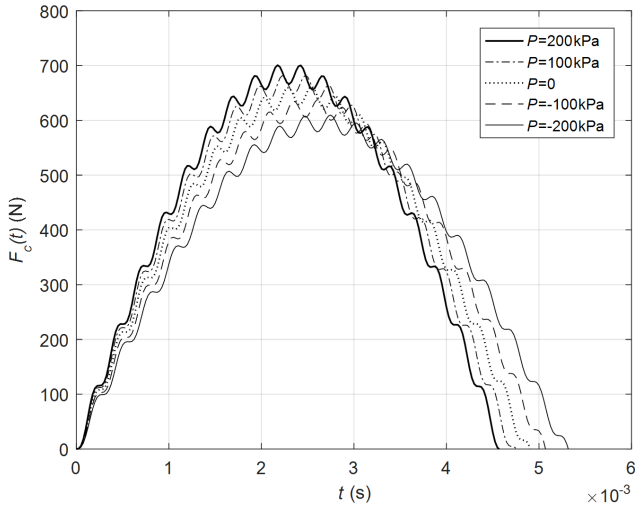

Fig. 19. Contact force in presence of the tensile pre-load $N_a = 200$kN/m and different pressures

The effect of different pressures on the shell response in the presence of the compressive pre-load $N_a = -200$kN/m are shown in Figs. 21 and 22 and the maximum numerical values are shown in Table 12. As can be seen, in the presence of compressive pre-load, the external pressure has more effects on the shell response rather than the internal pressure. As compared to the state where there is no pressure applied to the shell, by applying the external pressure $P = -200$kPa to the shell, the contact force decreases by 22.71% and the deflection increases by 23.89%, while the internal pressure P=200kPa increases the contact force by 10.7% and decreases the deflection by 11.63%. Similar to Figs. 19 and 20, regardless of the sign of the lateral pressure, P, the overall stiffness of the shell changes by applying either positive or negative initial stress in the axial direction, N_a.

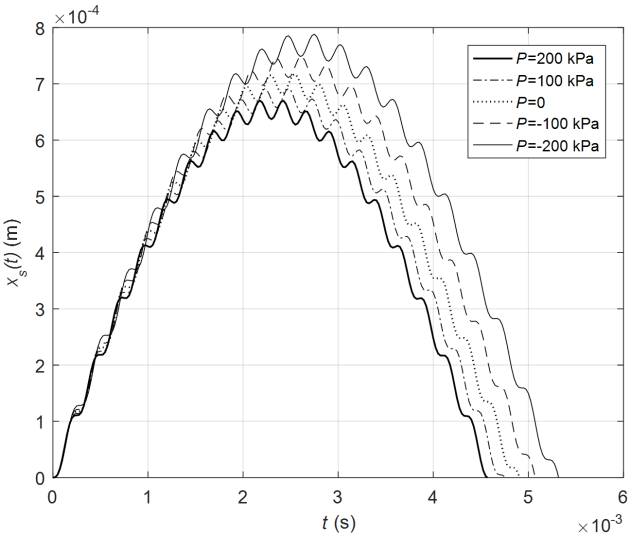

Fig. 20. Deflection of the shell in presence of the tensile pre-load $N_a = 200$kN/m and different pressures.

The percentage of relative changes (δ) in the max-

imum contact force, the maximum deflection and the contact time versus temperature differences as compared to the case where no temperature is applied to the shell, are shown in Fig. 23. In this figure, it can be seen that the effect of the initial temperature difference on the shell response is greater when the axial pre-load is compressive.

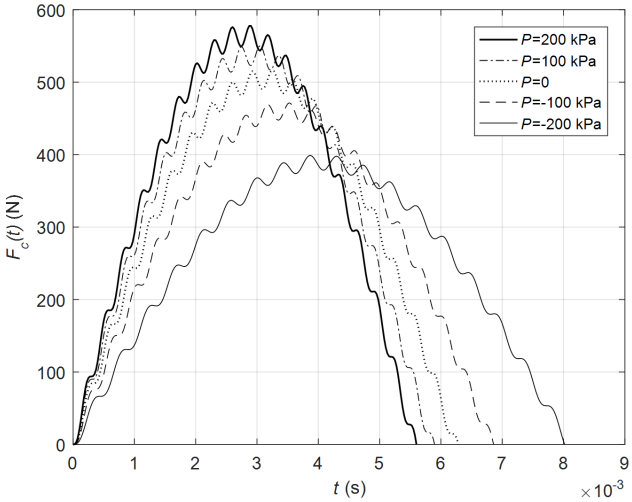

Fig. 21. Contact force in presence of the compressive pre-load $N_a = -200$kN/m and different pressures.

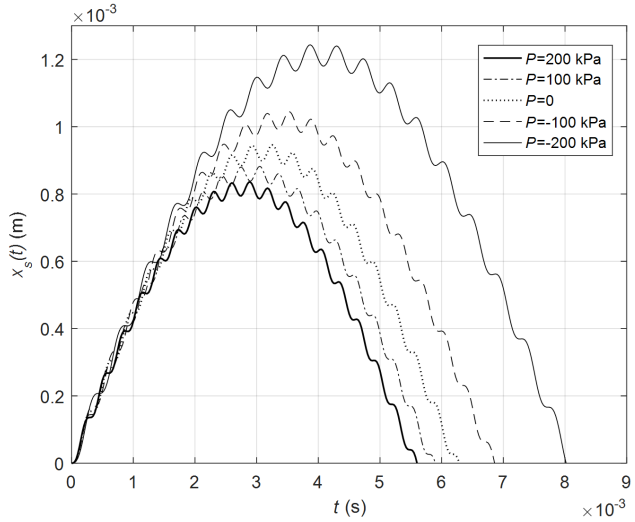

Fig. 22. Deflection of the shell in presence of the compressive pre-load $N_a = 200$kN/m and different pressures.

The percentage of relative changes (δ) in the maximum contact force, the maximum deflection and the contact time versus radial pressures relative to the case where no pressure is applied to the shell is shown in Fig. 24. Making comparison between Figs. 23 and 24 reveals that generally, the initial pressure has a greater effect on the shell response rather than the initial temperature difference, especially when the axial pre-load is compressive. Regardless of the type of the axial pre-load (tensile or compressive), the variation of δ with respect to the initial temperature difference is almost linear as indicated in Fig. 23. Furthermore, as shown in Fig. 24, for tensile axial pre-load, the variation of δ with respect to the radial pressure is almost linear. But, for the compressive axial pre-load, the variation of δ with respect to the radial pressure is nonlinear. For example, the maximum shell deflection is affected by about 30% when the external radial pressure is -200kPa and the axial compressive pre-load is -200kN/m.

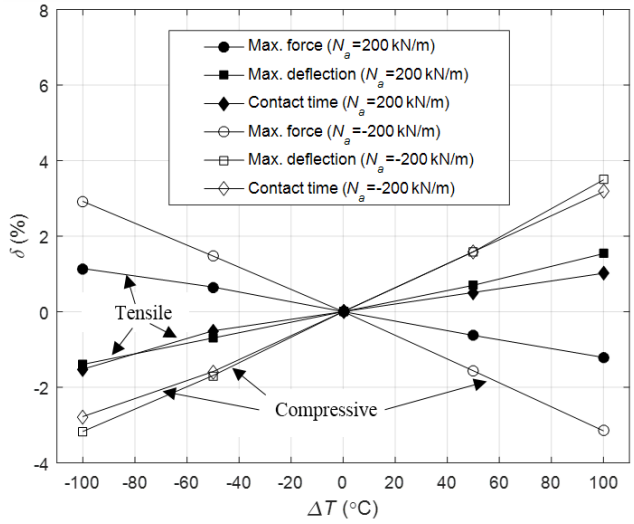

Fig. 23. The percentage of relative changes vs. temperature difference in presence of the tensile and compressive axial pre-loads.

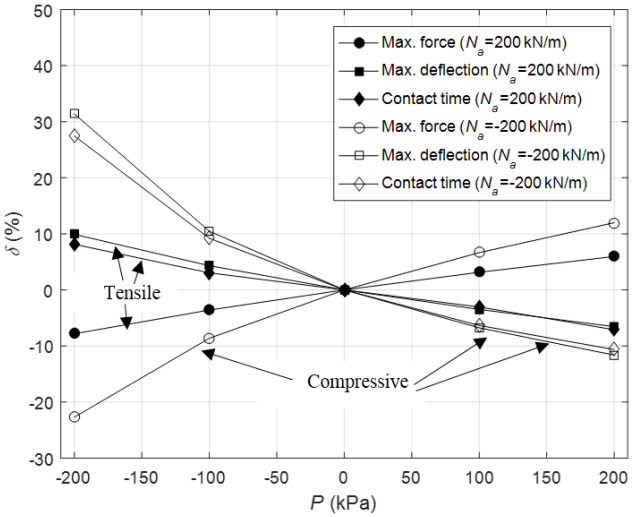

Fig. 24. The percentage of relative changes vs. radial pressure in presence of the tensile and compressive axial pre-loads.

7. Conclusions

In this paper, the low-velocity impact response of composite cylindrical shells in the presence of the combined mechanical and thermal pre-loads was investi-

gated. The time function of the contact force was obtained using a Two-Degree-of-Freedom (TDOF) model. The results showed that the temperature changes can change the shell's impact response. The positive temperature difference, compressive axial pre-load and external pressure cause the maximum contact force to decrease and the maximum deflection and the contact time to increase. Vice versa, the negative temperature difference, tensile axial pre-load and internal pressure cause the maximum contact force to increase and the maximum deflection and the contact time to decrease. The parameter (δ) was defined as the percentage of the relative changes in the maximum contact force, the maximum deflection and the contact time. Regardless of the type of the axial pre-load (tensile or compressive), the variation of δ with respect to the initial temperature difference is almost linear. Furthermore, the variation of δ with respect to the radial pressure is almost linear for tensile axial pre-load, but it is nonlinear for the compressive axial pre-load.

Appendix A

Differential operators L_{ij} used in Eq. (9):

$$L_{11} = A_{11}\frac{\partial^2}{\partial x^2} + A_{66}\frac{1}{R^2}\frac{\partial^2}{\partial \varphi^2} + \frac{P}{R}\frac{\partial^2}{\partial \varphi^2} - I_1\frac{\partial^2}{\partial t^2}$$

$$L_{12} = L_{21} = A_{12}\frac{1}{R}\frac{\partial^2}{\partial x \partial \varphi} + A_{66}\frac{1}{R}\frac{\partial^2}{\partial x \partial \varphi}$$

$$L_{13} = -L_{31} = \left(\frac{A_{12}}{R} + P\right)\frac{\partial}{\partial x}$$

$$L_{14} = L_{41} = B_{11}\frac{\partial^2}{\partial x^2} + B_{66}\frac{1}{R^2}\frac{\partial^2}{\partial \varphi^2} - I_2\frac{\partial^2}{\partial t^2}$$

$$L_{15} = L_{51} = (B_{12} + B_{66})\frac{1}{R}\frac{\partial^2}{\partial x \partial \varphi}$$

$$L_{22} = A_{22}\frac{1}{R^2}\frac{\partial^2}{\partial \varphi^2} + (A_{66} + N_a - N_x^T)\frac{\partial^2}{\partial x^2} + \frac{P}{R}\frac{\partial^2}{\partial \varphi^2} - \frac{H_{55}}{R^2} - \left(I_1 + \frac{2I_2}{R}\right)\frac{\partial^2}{\partial t^2}$$

$$L_{23} = -L_{32} = \left(\frac{A_{22}}{R^2} + \frac{H_{55}}{R^2} + P\right)\frac{\partial}{\partial \varphi}$$

$$L_{24} = L_{42} = (B_{12} + B_{66})\frac{1}{R}\frac{\partial^2}{\partial x \partial \varphi}$$

$$L_{25} = L_{52} = B_{22}\frac{1}{R^2}\frac{\partial^2}{\partial \varphi^2} + B_{66}\frac{\partial^2}{\partial x^2} + \frac{H_{55}}{R} - \left(I_2 + \frac{I_3}{R}\right)\frac{\partial^2}{\partial t^2}$$

$$L_{33} = (H_{44} + N_a - N_x^T)\frac{\partial^2}{\partial x^2} + (H_{55} - N_\varphi^T + PR)\frac{1}{R^2}\frac{\partial^2}{\partial \varphi^2} - 2N_{x\varphi}^T\frac{1}{R}\frac{\partial^2}{\partial x \partial \varphi} - \frac{A_{22}}{R^2} - I_1\frac{\partial^2}{\partial t^2}$$

$$L_{34} = -L_{43} = \left(H_{44} - \frac{B_{12}}{R}\right)\frac{\partial}{\partial x}$$

$$L_{35} = -L_{53} = \left(\frac{RH_{55} - B_{22}}{R^2}\right)\frac{\partial}{\partial \varphi}$$

$$L_{44} = D_{11}\frac{\partial^2}{\partial x^2} + D_{66}\frac{1}{R^2}\frac{\partial^2}{\partial \varphi^2} - H_{44} - I_3\frac{\partial^2}{\partial t^2}$$

$$L_{45} = L_{54} = (D_{12} + D_{66})\frac{1}{R}\frac{\partial^2}{\partial x \partial \varphi}$$

$$L_{55} = D_{22}\frac{1}{R^2}\frac{\partial^2}{\partial \varphi^2} + D_{66}\frac{\partial^2}{\partial x^2} - H_{55} - I_3\frac{\partial^2}{\partial t^2}$$

Appendix B

Mass matrix and stiffness matrix components used in Eq. 12:

$$M_{11} = M_{33} = I_1 \quad M_{22} = I_1 + \frac{2I_2}{R} \quad M_{44} = M_{55} = I_3$$

$$M_{14} = M_{41} = I_2 \quad M_{25} = M_{52} = I_2 + \frac{I_3}{R}$$

$$M_{12} = M_{13} = M_{15} = M_{21} = M_{23} = M_{24} = M_{31} = M_{32} = M_{34} = M_{35} = M_{42} = M_{43} = M_{45} = M_{51} = M_{53} = M_{54} = 0$$

$$\left(\alpha = \frac{m\pi}{l_x}, \quad \beta = \frac{n\pi}{\gamma}\right)$$

$$K_{11} = A_{11}\alpha^2 + (A_{66} + PR)\frac{\beta^2}{R^2}$$

$$K_{12} = K_{21} = \frac{\alpha\beta}{R}(A_{12} + A_{66})$$

$$K_{13} = K_{31} = -\alpha\left(\frac{A_{12}}{R} + P\right)$$

$$K_{14} = K_{41} = B_{11}\alpha^2 + B_{66}\frac{\beta^2}{R^2}$$

$$K_{15} = K_{51} = \frac{\alpha\beta}{R}(B_{12} + B_{66})$$

$$K_{22} = (A_{66} + N_a - N_x^T)\alpha^2 + (A_{22} + PR)\frac{\beta^2}{R^2} + \frac{H_{55}}{R^2}$$

$$K_{23} = K_{32} = -\frac{\beta}{R^2}(A_{22} + PR^2 + H_{55})$$

$$K_{24} = K_{42} = \frac{\alpha\beta}{R}(B_{12} + B_{66})$$

$$K_{25} = K_{52} = B_{66}\alpha^2 + B_{22}\frac{\beta^2}{R^2} - \frac{H_{55}}{R}$$

$$K_{33} = (H_{44} + N_a - N_x^T)\alpha^2 + (H_{55} + PR)\frac{\beta^2}{R^2} + \frac{A_{22}}{R^2}$$

$$K_{34} = K_{43} = \frac{\alpha}{R}(RH_{44} - B_{12})$$

$$K_{35} = K_{53} = \frac{\beta}{R^2}(RH_{55} - B_{22})$$

$$K_{44} = D_{11}\alpha^2 + D_{66}\frac{\beta^2}{R^2} + H_{44}$$

$$K_{45} = K_{54} = \frac{\alpha\beta}{R}(D_{12} + D_{66})$$

$$K_{55} = D_{66}\alpha^2 + D_{22}\frac{\beta^2}{R^2} + H_{55}$$

References

[1] S.W. Gong, S.L. Toh, V.P.W. Shim, The elastic response of orthotropic laminated cylindrical shells to low-velocity impact, Compos. Eng., 4(2) (1994) 247-266.

[2] S.L. Toh, S.W. Gong, V.P.W. Shim, Transient stresses generated by low-velocity impact on orthotropic laminated cylindrical shells, Compos. Struct., 31(3) (1995) 213-228.

[3] S.A. Matemilola, W.J. Stronge, Impact response of composite cylinders, Int. J. Solids Struct., 34(21) (1997) 2669-2684.

[4] S. Abrate, Modeling of impacts on composite structures, Compos. Struct., 51(2) (2001) 129-138.

[5] S.C. Her, Y.C. Liang, The finite element analysis of composite laminates and shell structures subjected to low velocity impact, Compos. Struct., 66(1-4) (2004) 277-285.

[6] S. Kumar, B. Nageswara Rao, B. Pradhan, Effect of impactor parameters and laminate characteristics on impact response and damage in curved composite laminates, J. Reinf. Plast. Compos., 26(13) (2007) 1273-1290.

[7] H. Saghafi, G. Minak, A. Zucchelli, Effect of preload on the impact response of curved composite panels. Compos. B Eng., 60 (2014) 74-81.

[8] I.H. Choi, Geometrically nonlinear transient analysis of composite laminated plate and shells subjected to low-velocity impact, Compos. Struct., 142 (2016) 7-14.

[9] F. Najafi, M.H. Shojaeefard, H. Saeidi Googarchin, Low-velocity impact response of functionally graded doubly curved panels with Winkler-Pasternak elastic foundation: an analytical approach, Compos. Struct., 162 (2017) 351-364.

[10] R. Rafiee, A. Ghorbanhosseini, S. Rezaee, Theoretical and numerical analyses of composite cylinders subjected to the low-velocity impact, Compos. Struct., 226 (2019) 111230.

[11] T. Langella, A. Rogani, P. Navarro, J.F. Ferrero, V. Lopresto, A. Langella, Experimental study of the influence of a tensile preload on thin woven composite laminates under impact loading, J. Mater. Eng. Perform., 28(6) (2019) 3203-3210.

[12] W. Harris, C. Soutis, C. Atkin, Impact response of curved composite laminates: effect of radius and thickness, Appl. Compos. Mater., 27(5) (2020) 555-573.

[13] B. Liao, Y. Du, J. Zheng, D. Wang, Y. Lin, R. Tao, C. Zhou, Prediction of residual burst strength for composite pressure vessels after low velocity impact, Int. J. Hydrog. Energy, 45(18) (2020) 10962-10976.

[14] R. Rafiee, H. Rashedi, S. Rezaee, Theoretical study of failure in composite pressure vessels subjected to low-velocity impact and internal pressure, Front. Struct. Civ. Eng., 14(6) (2020) 1349-1358.

[15] K.P. Soldatos, V.P. Hadjigeorgiou, Three-dimensional solution of the free vibration problem of homogeneous isotropic cylindrical shells and panels, J. Sound Vib., 137(3) (1990) 369-384.

[16] S.M.R. Khalili, K. Malekzadeh, A. Davar, P. Mahajan, Dynamic response of pre-stressed fiber metal laminate (FML) circular cylindrical shells subjected to lateral pressure pulse loads, Compos. Struct., 92(6) (2010) 1308-1317.

[17] G.G. Sheng, X. Wang, Thermal vibration, buckling and dynamic stability of functionally graded cylindrical shells embedded in an elastic medium, J. Reinf. Plast. Compos., 27(2) (2008) 117-134.

[18] R.M. Jones, Mechanics of Composite Materials, 2nd Ed., Taylor Francis, Virginia, (1998).

[19] C.W. Bert, M. Kumar, Vibration of cylindrical shells of bimodulus composite materials, J. Sound Vib., 81(1) (1982) 107-121.

[20] L. Meirovitch, Fundamentals of Vibrations. McGraw-Hill Publisher, (2001).

[21] T. Vodenitcharova, P. Ansourian, Buckling of circular cylindrical shells subject to uniform lateral pressure, Eng. Struct., 18(8) (1996) 604-614.

[22] J.L. Mantari, A.S. Oktem, C. Guedes Soares, Static and dynamic analysis of laminated composite and sandwich plates and shells by using a new higher-order shear deformation theory, Compos. Struct., 94(1) (2011) 37-49.

[23] S.R. Swanson, Limits of quasi-static solutions in impact of composite structures, Compos. Eng., 2(4) (1992) 261-267.

[24] I.H. Choi, C.H. Lim, Low-velocity impact analysis of composite laminates using linearized contact law, Compos. Struct., 66(1-4) (2004) 125-132.

[25] S.M.R. Khalili, M. Soroush, A. Davar, O. Rahmani, Finite element modeling of low-velocity impact on laminated composite plates and cylindrical shells, Compos. Struct., 93(5) (2011) 1363-1375.

[26] X. Zhao, K.M. Liew, T.Y. Ng, Vibration analysis of laminated composite cylindrical panels via a meshfree approach, Int. J. Solids Struct., 40(1) (2003) 161-180.

[27] K.P. Soldatos, A comparison of some shell theories used for the dynamic analysis of cross-ply laminated circular cylindrical panels, J. Sound Vib., 97(2) (1984) 305-319.

[28] R. Azarafza, S.M.R. Khalili, A.A. Jafari, A. Davar, Analysis and optimization of laminated composite circular cylindrical shell subjected to compressive axial and transverse transient dynamic loads, Thin-Walled Struct., 47(8-9) (2009) 970-983.

[29] B. Mirzavand, M.R. Eslami, Thermal buckling of imperfect functionally graded cylindrical shells based on the Wan–Donnell model, J. Therm. Stresses, 29(1) (2006) 37-55.

[30] E. Asadi, W. Wang, M.S. Qatu, Static and vibration analyses of thick deep laminated cylindrical shells using 3D and various shear deformation theories, Compos. Struct., 94(2) (2012) 494-500.

[31] L.S. Kistler, A.M. Waas, Experiment and analysis on the response of curved laminated composite panels subjected to low-velocity impact, Int. J. Impact. Eng., 21(9) (1998) 711-736.

[32] M.O. Pierson, R. Vaziri, Analytical solution for low-velocity impact response of composite plates, AIAA J., 34(8) (1996) 1633-1640.